APPLIED SCIENCES AND ENGINEERING

Metal-polyDNA nanoparticles reconstruct osteoporotic microenvironment for enhanced osteoporosis treatment

Xueliang Liu[1]†, Fan Li[2]†, Ziliang Dong[3], Chao Gu[1,4], Dongsheng Mao[1], Jingqi Chen[1], Lei Luo[1], Yuting Huang[1], Jie Xiao[5]*, Zhanchun Li[2]*, Zhuang Liu[3]*, Yu Yang[1]*

Current clinical approaches to osteoporosis primarily target osteoclast biology, overlooking the synergistic role of bone cells, immune cells, cytokines, and inorganic components in creating an abnormal osteoporotic microenvironment. Here, metal-polyDNA nanoparticles (Ca-polyCpG MDNs) composed of Ca^{2+} and ultralong single-stranded CpG sequences were developed to reconstruct the osteoporotic microenvironment and suppress osteoporosis. Ca-polyCpG MDNs can neutralize osteoclast-secreted hydrogen ions, provide calcium repletion, promote remineralization, and repair bone defects. Besides, the immune-adjuvant polyCpG in MDNs could induce the secretion of osteoclastogenesis inhibitor interleukin-12 and reduce the expression of osteoclast function effector protein to inhibit osteoclast differentiation, further reducing osteoclast-mediated bone resorption. PPi^{4-} generated during the rolling circle amplification reaction acts as bisphosphonate analog and enhances bone targeting of Ca-polyCpG MDNs. In ovariectomized mouse and rabbit models, Ca-polyCpG MDNs prevented bone resorption and promoted bone repair by restoring the osteoporotic microenvironment, providing valuable insights into osteoporosis therapy.

INTRODUCTION

Osteoporosis is a silent skeletal disease characterized by low bone mass and microarchitectural deterioration of bone tissue, followed by an increased risk of bone fragility and fracture (*1*–*3*). During such disease progression, dysfunctional interactions between various bone cells, inorganic components, immune cells, and various signaling proteins/cytokines in osteoporotic microenvironment often work together to ultimately generate osteoporosis (*3*–*5*). Osteoclasts, the key cells in the osteoporotic microenvironment, are responsible for bone resorption and can secrete acids and lytic enzymes to degrade bone minerals and collagen, leading to severe bone mineral loss (*6*, *7*). Although the compensatory formation of bone matrix and bone mineralization mediated by osteoblasts can alleviate bone mineral loss, the age-dependent calcium deficiency in the osteoporotic microenvironment limits the remineralization and repair of bone defects (*8*, *9*). In addition to bone cells and calcium, various immune cells with secreted cytokines including T cells, B cells, monocytes, and macrophages are also involved in the establishment of osteoporotic microenvironment during the pathogenesis of osteoporosis (*10*–*12*). However, current treatment options, which mostly use antiresorptive agents (e.g., estrogen, bisphosphonates, and denosumab) in a single modality, cannot regulate the osteoporotic microenvironment, thereby limiting its efficacy of osteoporosis treatment (*13*, *14*). Thus, the development of a multimodal cocktail-like treatment to reconstruct the entire osteoporotic microenvironment and restore bone mass balance may contribute to a more rational and comprehensive osteoporosis treatment strategy.

Besides antiresorptive agents, bioactive nanomaterials offer an efficient alternative for the potential osteoporosis treatment and stimulating bone regeneration (*15*, *16*). First, as carriers for efficient therapeutic delivery, nanoparticles showed enhanced intracellular delivery and improved bioavailability of therapeutic (*17*–*19*). In addition, for bone tissue regeneration, nanomaterials are characterized by large surface area and roughness, which facilitate their interaction with neighboring proteins, cells, and inorganic components in the osteoporotic microenvironment (*20*). For instance, mineral-based therapeutics using calcium-based materials [e.g., calcium phosphate, hydroxyapatite (HAP), or bisphosphonates] can induce osteoblast differentiation of cells and promote bone tissue regeneration (*21*, *22*). However, to the best of our knowledge, previous research reports have focused on drug delivery (*23*), the anti-bone resorption (*24*), and bone repair potency (*21*, *25*) of the nanomaterials, with few efforts on the universal osteoporotic microenvironment reconstruction, severely limiting their clinical treatment effect for osteoporosis. Therefore, there is an urgent need for the on-demand design of safer and more effective nanomedicine to restore the complex microenvironment in osteoporosis for osteoporosis treatment.

Metal-organic frameworks (MOFs) consisting of metal ions coordinated by small organic ligands have attracted considerable attention in biological applications due to their well-defined sizes/shapes and structural/chemical diversity (*26*–*29*). However, owing to the simplex function, using small organic ligands to construct MOFs/coordination polymers extremely limits the on-demand design of multifunctional MOFs in the field of biomedicine. Recently, we and others have used biomacromolecules (e.g., DNA and RNA) instead of small organic molecules as bridge ligands to

[1]Institute of Molecular Medicine (IMM), Renji Hospital, School of Medicine, Shanghai Jiao Tong University, Shanghai 200240, China. [2]Institute of Functional Nano & Soft Materials Laboratory (FUNSOM), Soochow University, Suzhou, Jiangsu 215123, China. [3]Department of Orthopaedic Surgery, Renji Hospital, School of Medicine, Shanghai Jiao Tong University, Shanghai 200127, China. [4]Department of Anesthesiology, Renji Hospital, School of Medicine, Shanghai Jiao Tong University, Shanghai 200127, China. [5]Department of Thoracic Surgery, Shanghai Pulmonary Hospital, School of Medicine, Tongji University, Shanghai 200433, China.
*Corresponding author. Email: yuyang@shsmu.edu.cn (Y.Y.); zliu@suda.edu.cn (Z. Liu); lzctgzyyx@163.com (Z. Li); applexiaomz@163.com (J.X.)
†These authors contributed equally to this work.

customize multifunctional metal-DNA/RNA nanoparticles by chelating metal ions (*30*–*34*). However, metal-DNA/RNA nanoparticles composed of the monovalent functional nucleic acids showed poor stability and affinity in the biological environments (*35*–*37*). To this end, polynucleotide DNA (polyDNA), a kind of ultralong single-stranded DNA (ssDNA) with polyvalent functional DNA sequences and improved stability, is proposed to coordinate with metal ions to form multifunctional metal-polyDNA nanoparticles (MDNs). With their on-demand design, programmable flexibility, and diverse functionalities, MDNs are expected to provide unprecedented opportunities for biomedical applications.

Here, we customize multifunctional MDNs to regulate the entire osteoporotic microenvironment for osteoporosis treatment. As a proof of concept, long ssDNA containing polynucleotide CpG (polyCpG) sequences synthesized by rolling circle amplification (RCA) was coordinated with calcium ions to prepare functional MDNs (Fig. 1A). First, Ca-polyCpG MDNs could neutralize osteoclast-secreted hydrogen ions to inhibit the mature osteoclast-mediated bone erosion and, triggered by the osteoporotic acidic microenvironment, can release Ca^{2+} to improve bone mineralization and enhance bone repair (Fig. 1B). Second, the polyCpG sequences could induce the synthesis and release of interleukin-12 (IL-12), which is a cytokine known to inhibit osteoclast differentiation, and reduce the expression of osteoclast function effector protein to reduce bone resorption. In addition, naturally occurring pyrophosphates (PPi^{4-}) produced in the RCA process are analogs of the antiresorptive agent bisphosphonates, which could enhance the targeting and retention time of the MDNs to the bone and enhance calcium supplementation–based bone mineralization. Notably, we demonstrated that Ca-polyCpG MDNs, after local and systematic administration, could restore damaged bone to nearly normal levels within a month in both ovariectomy (OVX)–induced mouse and rabbit models of osteoporosis. Our work thus presents a general platform with an on-demand design for osteoporosis therapy through reconstruction of the osteoporotic environment.

RESULTS

The design and characterizations of Ca-polyCpG MDNs

In our design, a liner oligonucleotide complementary to the CpG sequence (table S1) was looped by T4 DNA ligase to generate a circular template. Then, followed by a typical RCA reaction in the presence of the template and phi29 DNA polymerase, a long ssDNA containing polymeric CpG (polyCpG) sequences was synthesized (Fig. 1A). Agarose gel electrophoresis confirmed the formation of each product, with the polyCpG strands migrating slower than others (Fig. 1C), indicating high amplification efficiency to synthesize the ultralong polyDNA (fig. S1). To verify the generated polyCpG, Cy5-labeled complementary chains of CpG were added to the RCA reaction solution. With the increase of reaction time, the fluorescence intensity of Cy5 of polyCpG gradually increased, further confirming the generation of the long single-stranded polyCpG during the RCA process (Fig. 1D and fig. S2).

After the RCA process, $CaCl_2$ was added to coordinate with polyCpG, leading to the formation of MDNs. Dynamic light scattering (DLS) indicated increased particle size of Ca-polyCpG MDNs along with prolonged time, reaching about 300 nm at 2 hours (Fig. 1D and fig. S3A). When the reaction was performed for 4 hours, however, MDNs became too large with greater nonuniformity in size (fig. S3B). Thus, we chose 2 hours as the optimal reaction time to synthesize Ca-polyCpG MDNs in the following experiments. As shown in scanning electron microscopy (SEM) and transmission electron microscopy (TEM) imaging, such Ca-polyCpG MDNs displayed monodispersed morphology and porous structures (Fig. 1, E and F). Element mapping analysis of high-angle annular dark-field scanning TEM (HAADF-STEM) revealed that the Ca and P elements were randomly distributed in Ca-polyCpG MDNs (Fig. 1G and fig. S4), confirming the successful synthesis of Ca-polyCpG MDNs. The loading capacity of Ca^{2+} in the synthetic Ca-polyCpG MDNs was evaluated using the Calcium Colorimetric Assay Kit. To determine the loading efficiency of DNA, the nanostructure of Ca-polyCpG MDNs was disrupted using EDTA, and the concentrations of DNA were then measured using an ultraviolet-visible spectrophotometer. After careful calculations, the loading efficiencies of DNA and Ca^{2+} in the synthetic Ca-polyCpG MDNs were determined to be 37.0 and 21.7%, respectively.

The physiological and anti-enzymatic cleavage stability of Ca-polyCpG MDNs was then evaluated. After 7 days of incubation in water, the particle size and dispersion of Ca-polyCpG MDNs did not change notably (fig. S5), indicating the excellent storage stability of those nanoparticles. Next, Ca-polyCpG MDNs and free CpG were both incubated with deoxyribonuclease I (DNase I) solution or serum for different time periods, in which Ca-polyCpG MDNs exhibited no obvious degradation within 72 hours, while most free CpG degraded within 0.5 hours in DNase I solution and 3 hours in serum (Fig. 1H). These results indicated that Ca-polyCpG MDNs could greatly enhance the stability of the CpG in blood and intracellular DNA enzyme environment. In addition, the hemolytic assay showed that Ca-polyCpG MDNs did not cause visual hemolysis with a hemolysis rate of less than 3% (fig. S6), indicating the good hemocompatibility of Ca-polyCpG MDNs.

Ca-polyCpG MDN–mediated acid neutralization and bone remineralization in vitro

HAP [$Ca_{10}(PO_4)_6(OH)_2$], the major component of the hierarchical bone issue, is severely lost in the osteoporotic microenvironment (*38*). Although many biomaterials have been developed for the repair of bone defects, the special collagen fibril structure of the bone (e.g., only 1.8 to 4 nm tortuous subchannels) limited the delivery of therapeutics, thereby making it difficult to induce the recovery of the affected bone (*39*). Notably, our Ca-polyCpG MDNs were able to be decomposed in an acidic-osteoporotic environment to release free Ca^{2+} (*40*), which would show deeper penetration into collagen fibrils of the bone issues to allow bone mineralization (*41*). To evaluate the pH-responsive release properties, Ca-polyCpG MDNs were treated with phosphate-buffered saline (PBS) at pH 7.4 and 5.0. The TEM images showed that the uniform structure of Ca-polyCpG MDNs could maintain at pH 7.4, but completely collapse at pH 5.5 in 30 min (Fig. 2A). Next, the Ca^{2+} release profile of Ca-polyCpG MDNs at pH 7.4 and pH 5.0 was well determined with the Calcium Colorimetric Assay Kit (*42*). At pH 5.0, up to 80% of the Ca^{2+} ions in Ca-polyCpG MDNs were released within 12 hours, while at pH 7.4, little Ca^{2+} ions were released (Fig. 2B and fig. S7). To investigate the importance of the regulation of acid microenvironments of Ca-polyCpG MDNs, we chose Mg-polyCpG MDNs as a control group, which was synthesized using Mg^{2+} instead of Ca^{2+}. When a titration was performed with 0.5%

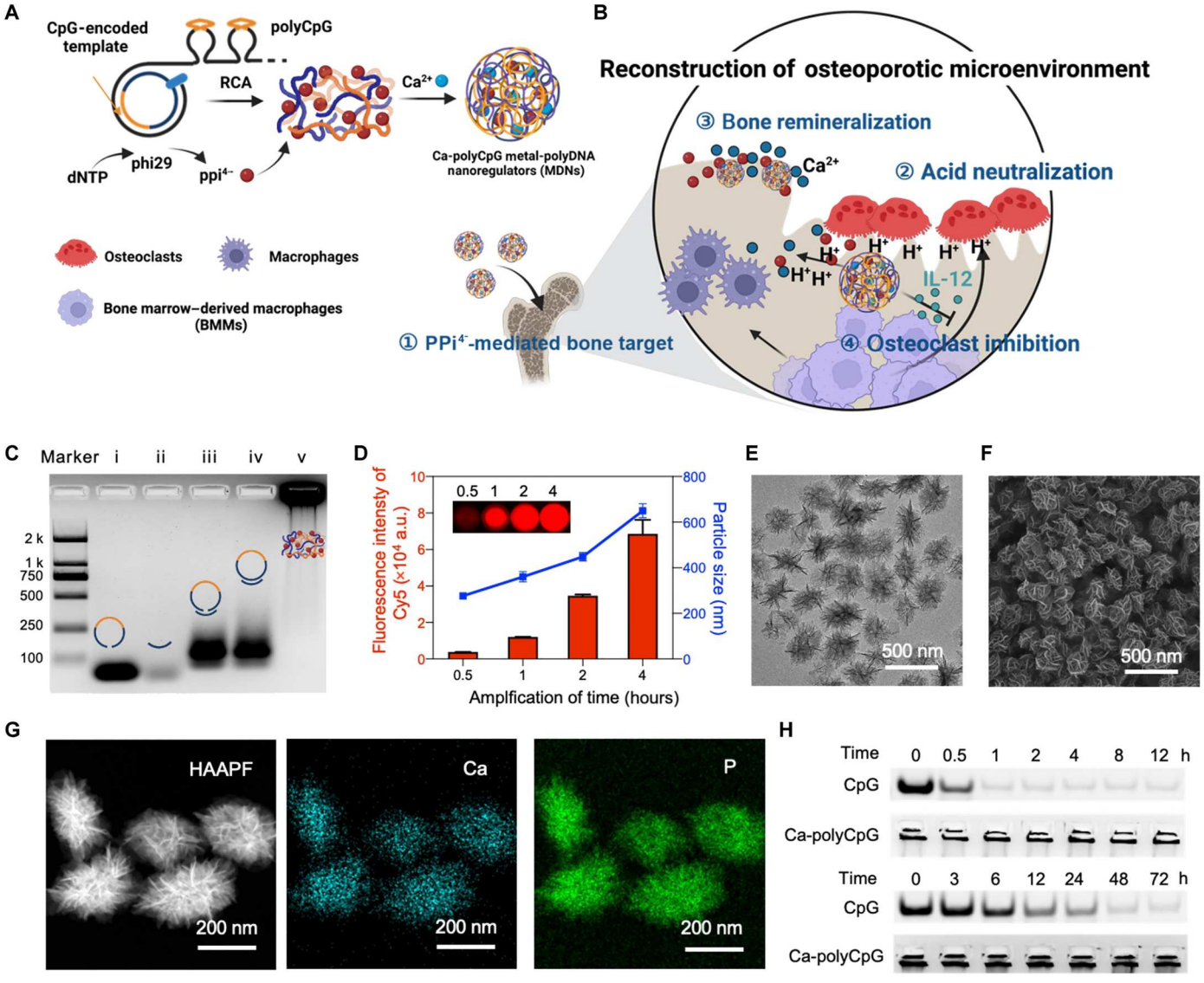

Fig. 1. Preparation and characterization of Ca-polyCpG MDNs. (**A**) Schematic illustration of the preparation of Ca-polyCpG MDNs by coordination of Ca^{2+} and polyCpG, the latter of which were synthesized by the RCA reaction. (**B**) Schematic representation of Ca-polyCpG MDN–based reconstruction of the osteoporotic microenvironment. Ca-polyCpG MDNs with ability to target calcium elements, promote M1 macrophage polarization, and inhibit osteoclast activity can reconstruct the osteoporotic microenvironment to treat osteoporosis. (**C**) Agarose gel electrophoresis of DNA ladder (i), template (ii), primer (iii), circular DNA (iv), closed circular DNA (v), and polyCpG (vi). (**D**) Particle sizes and fluorescence changes of polyCpG during RCA reaction at different time points ($n = 3$). For fluorescence measurement, Cy5-labeled complementary DNA was added to the RCA reaction solution to label the generated polyCpG. (**E**) TEM and (**F**) SEM images of Ca-polyCpG MDNs. Scale bar, 500 nm. (**G**) HAADF-STEM image and corresponding element mapping analysis of Ca-polyCpG MDNs. Scale bar, 200 nm. (**H**) Gel electrophoresis showed the stability of free CpG and Ca-polyCpG MDNs after incubation in DNase I (top) and serum (bottom) environments at different time points. a.u., arbitrary units.

hydrochloric acid, we found that Ca-polyCpG MDNs and Mg-polyCpG MDNs could notably slow down the pH decrease (Fig. 2C), reflecting the pH-responsive and superior acid-resistant properties.

As a critical factor in bone resorption, mature osteoclasts adhere to the bone surface and secrete large amounts of hydrogen ions (H^+) to acidify the local extracellular microenvironment, which dissolves the mineral phase of bone and provides an optimal environment for organic matrix degradation. Given the critical role of acidification effects in osteoclastic bone resorption, Ca-polyCpG MDNs are expected to neutralize acid to inhibit osteoporosis. To confirm the local pH value in osteoporotic bones and extracellular acid–resistant property of Ca-polyCpG during osteoclast-mediated H^+ external secretion, we evaluated the fluorescence intensity of the pH probe fluorescein isothiocyanate (FITC; which exhibits fluorescence quenching at low pH values) on the bone surface after seeding osteoclasts labeled with DiI (1,1′-dioctadecyl-3,3,3′,3′-tetramethylindocarbocyanine perchlorate) (*18*). The results showed that, with the protection of Ca-polyCpG, the obvious green fluorescence signals were well maintained when DiI and 4′,6-diamidino-2-phenylindole (DAPI)–labeled osteoclasts adhered onto the bone surface (Fig. 2D and fig. S9). In contrast, the FITC signals almost disappeared when

osteoclasts were acid-etched. Furthermore, on the basis of the standard fluorescence intensity of FITC to pH value on the bone surface (fig. S8), we calculated the pH value within the acidic milieu of osteoclasts and found that Ca-polyCpG acting on the acidified area of osteoclasts showed higher pH value than the untreated osteoclasts group (pH 7 versus pH 5). In addition, similar to Ca-polyCpG, Mg-polyCpG can also maintain the green fluorescence signals when osteoclasts adhered onto the bone surface (fig. S9), indicating significant extracellular acid–resistant property. These results indicated that Ca-polyCpG could neutralize acid and maintain a relatively high local pH environment where osteoclasts secrete acid.

The capacity of Ca-polyCpG MDNs to enhance bone remineralization was evaluated on in vitro osteoporotic bone face by injecting a suspension of Ca-polyCpG MDNs. To investigate the capacity of pyrophosphates (PPi^{4-}) in Ca-polyCpG MDNs to enhance the affinity and retention time within bone tissues, we chose Ca-DNA nanoparticles as a control group, which was prepared by coordinated Ca^{2+} with nonfunctional long-stranded DNA (Herring sperm) in the absence of PPi^{4-} with similar size and zeta potential property to Ca-polyCpG MDNs (fig. S10) (*43*, *44*). After incubation with $CaCl_2$, Ca-DNA nanoparticles, or Ca-polyCpG MDNs at a concentration of 20 mM (in terms of Ca^{2+}) at 37°C for 2 weeks, the osteoporotic bones were analyzed by SEM. Some microporous structures in the

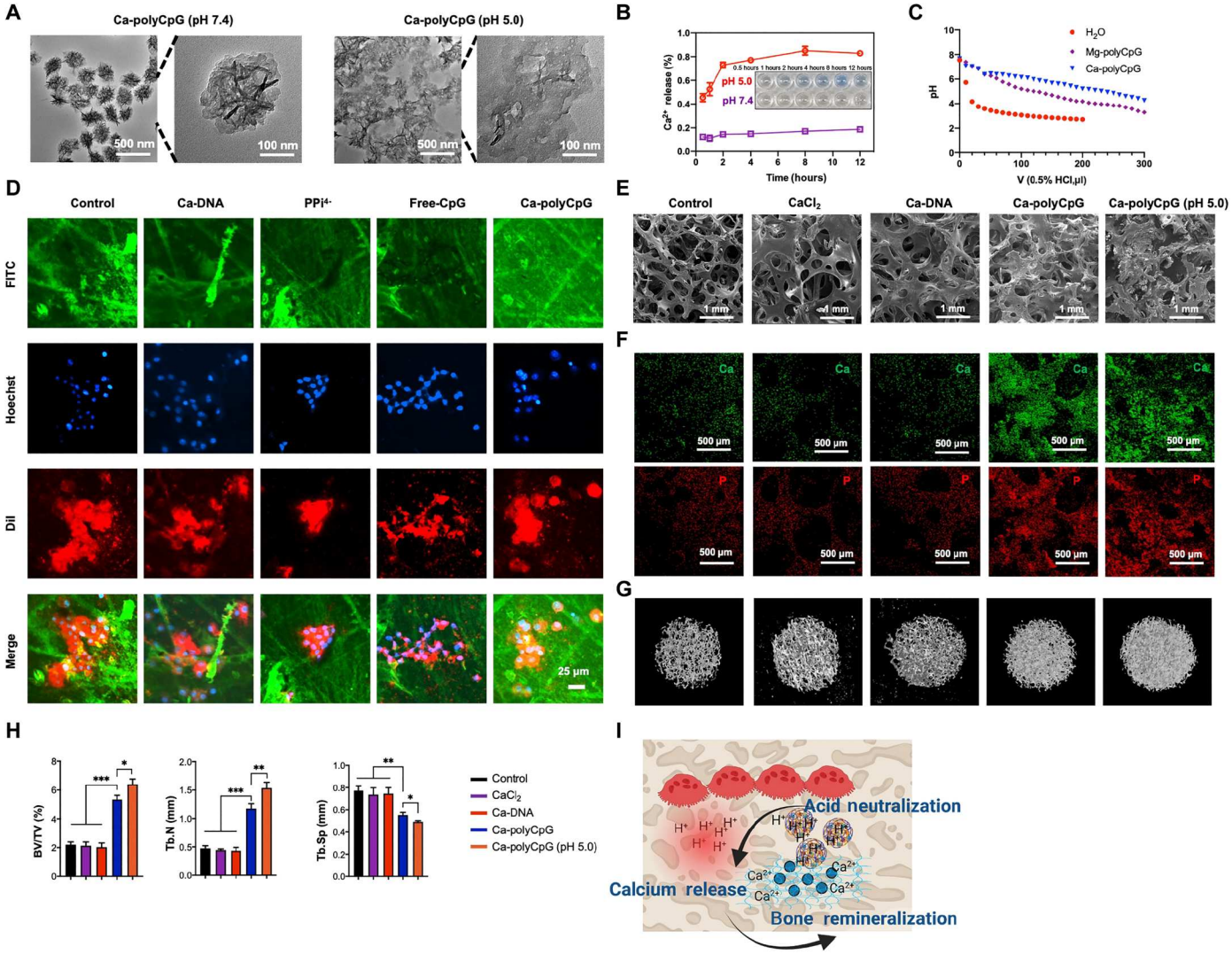

Fig. 2. In vitro results of osteoporotic bone and restored bone after treatment with Ca-polyCpG MDNs. (**A**) TEM images of Ca-polyCpG MDNs incubated at pH 5.0 and 7.4 for 30 min. Scale bar, 500 nm. (**B**) Ca^{2+} was released from Ca-polyCpG MDNs after incubation at pH 5.0 and 7.4 at different time points. $n = 3$. (**C**) pH values of Ca-polyCpG MDNs in the hydrochloric acid titration experiment. (**D**) Typical confocal images showing the extracellular acid resistance of Ca-polyCpG MDNs during osteoclast-mediated H^+ external secretion measured by pH indicator (fluorescence quenching at low pH). (**E** and **F**) Representative STEM and corresponding element mapping images of osteoporotic bone and recovered bone after various treatments [(i) PBS, (ii) $CaCl_2$, (iii) Ca-DNA (no PPi^{4-}), (iv) Ca-polyCpG MDNs, and (v) acid-treated Ca-polyCpG MDNs]. (**G**) Representative 3D micro-CT imaging of the osteoporotic bone and recovered bone after various treatments. (**H**) Quantitative results of the 3D micro-CT analysis expressed as the BV/TV, Tb.N, and Tb.Sp values. BV/TV, bone volume per tissue volume; Tb.N, trabecular number; Tb.Sp, trabecular separation ($n = 3$). (**I**) Schematic illustration of the acid neutralization, calcium release, and bone remineralization properties of MDNs in the osteoporotic microenvironment. Data are presented as means ± SD. $^*P < 0.05$, $^{**}P < 0.01$, and $^{***}P < 0.001$.

osteoporotic bone were observed after incubation of Ca-polyCpG MDNs at pH 7.4, whereas no obvious porous structures were observed after Ca-polyCpG MDN treatment and incubation at pH 5.0 (Fig. 2E). Besides, elemental mapping analysis of STEM showed that osteoporotic bone was deficient in calcium and phosphate, indicating the serious loss of HAP. However, Ca-polyCpG MDNs could substantially improve the calcium and phosphate content in the osteoporotic bone, especially after incubation at pH 5.0 (Fig. 2F).

In addition, we further characterized the surface morphology of the Ca-polyCpG MDN–treated osteoporotic bone by micro-computed tomography (micro-CT). The results indicated that free $CaCl_2$ and Ca-DNA (no PPi^{4-})–treated groups showed little bone recovery and appeared to be nearly similar to osteoporotic bone group (PBS) (Fig. 2G). In contrast, the Ca-polyCpG MDN group showed a clear recovery of osteoporotic bone with the thicker trabecular bone and narrower separation of trabecular. This notable improvement is because the PPi^{4-} component of Ca-polyCpG MDNs with a high affinity to the bone could increase the bone retention time of Ca-polyCpG MDNs, leading to enhanced bone mineralization. After incubation at pH 5.0, Ca-polyCpG MDNs exhibited the best salient bone mineralization with the notably reduced macroporous network in osteoporotic bone. This result is largely because the pH-triggered release of Ca^{2+} and PPi^{4-} showed better penetration into thick HAP crystalline, which promoted rapid adsorption to the bone surface and enhanced bone remineralization.

To further quantify the amount of newly recovered bone, histomorphometry was also used to assess the quantity of recovered bone. Compared to free Ca^{2+}–treated group, the value of the bone volume/tissue volume ratio (BV/TV) and trabecular number (Tb.N) in the Ca-polyCpG MDN group increased by 3.1- and 3.5-fold, respectively, and the value of the trabecular separation (Tb.Sp) reduced by 1.5-fold, indicating the superior performance of Ca-polyCpG MDNs in osteoporotic bone repair (Fig. 2H). Together, the above results demonstrated that Ca-polyCpG MDNs with excellent acid neutralization and pH-responsive Ca^{2+} release properties can effectively enhance bone remineralization to maintain the structural integrity of bone, especially in the acidic osteoporotic microenvironment (Fig. 2I).

Inhibiting osteoclast differentiation by Ca-polyCpG MDNs

Raw264.7 macrophage cells were first used to study cellular uptake of the free CpG and Ca-polyCpG MDNs. To track CpG, Ca-polyCpG MDNs were labeled by Cy5-labeled complementary sequence of CpG mentioned above, and the free CpG was labeled with the equal amount of Cy5 on its 5′ end. After 4 hours of incubation, the cellular uptake of the free CpG and Ca-polyCpG MDNs was visualized by confocal fluorescence microscopy and quantified by fluorescence-activated cell sorting (FACS) analysis. The Ca-polyCpG MDN group displayed a higher internalization in Raw264.7 cells with a 4.0-fold higher fluorescence intensity than the free CpG group (fig. S11). In addition, cell counting kit-8 (CCK-8) and calcein-AM/propidium iodide (PI) dual-staining assay showed that Ca-polyCpG MDNs had no detectable cytotoxicity on Raw264.7 cells, even at a concentration up to 100 nM (fig. S12). Furthermore, the bioactivity of osteoblasts was evaluated by alkaline phosphatase staining during their coculture with Ca-polyCpG MDNs to investigate the potential impact of MDNs on osteoblasts in the treatment of osteoporosis. The results showed that the presence of Ca-polyCpG MDNs did not induce any significant effect on osteogenesis (fig. S13).

Activating Toll-like receptor 9 (TLR9) in macrophage using CpG oligonucleotides has been found to be able to suppress receptor activator of nuclear factor κB (NF-κB) ligand (RANKL)–induced osteoclast formation in previous studies (*24*, *45*, *46*). Hence, we investigated whether functionalized Ca-polyCpG MDNs containing polyCpG were capable of inhibiting osteoclast differentiation and bone resorption activity. First, we studied osteoclast differentiation from the bone marrow–derived macrophages (BMMs), the most frequently used cell type in the research on osteoclastogenesis (*18*, *47*). Mouse femoral bone marrow cells were extracted and treated with macrophage colony-stimulating factor (M-CSF) for 3 days. Then, RANKL was used to induce the differentiation of BMMs to osteoclasts in the presence of Ca-polyCpG MDNs or free CpG. To evaluate the inhibitory effect of Ca-polyCpG MDNs on osteoclast differentiation, we first monitored the formation of the osteoclast actin ring, a critical protein in the maturation of osteoclasts (*48*). After stimulation by RANKL, BMMs were differentiated into mature osteoclasts with the expansion of cytoskeleton and formation of a more noticeable actin ring, which have bigger size than other cells (Fig. 3, A and B). Ca-polyCpG MDNs could dramatically shrink the actin ring to the size before RANKL treatment, which resulted in smaller cell size, indicating that Ca-polyCpG MDNs could suppress the development of the actin ring in mature osteoclasts (Fig. 3, A and B). Next, the effects of Ca-polyCpG MDNs on preosteoclast fusion were investigated by the double-stained fluorescence method (*49*). Briefly, BMMs were separated into two groups and then labeled with Hoechst (blue) for the nucleus and DiI (red) for the cell membrane, respectively. After coculturing the above two groups of cells in the presence of RANKL, cell fusion would be achieved and multinucleated osteoclasts would be formed. Ca-polyCpG MDNs could inhibit the formation of multinucleated osteoclasts (Fig. 3C). To further assess the proportion of osteoclasts differentiated from BMMs, the number of tartrate-resistant acid phosphatase (TRAP)–positive cells, a commonly used marker for osteoclasts, was quantified. Compared to that in the PBS group, the number and area of multinucleated osteoclasts in the Ca-polyCpG MDN group were significantly reduced (Fig. 3, D and E).

The anti-osteoclastic activities of CpG are attributed to the synthesis and release of IL-12, a cytokine known to inhibit osteoclast differentiation, after the activation of TLR9 (*46*). In addition, IL-12 can effectively inhibit RANKL-induced osteoclast differentiation by reducing RANKL-induced protein expression, such as nuclear factor of activated T cells cytoplasmic 1 (NFATc1) and c-Fos (*50*). To investigate the mechanism of Ca-polyCpG MDNs on osteoclast inhibition, we added Ca-DNA, a friendly MOF assembled by Ca^{2+} and nonfunctional long ssDNA, as a control group, and studied the effect of Ca-polyCpG MDNs on the secretion of IL-12 by monocytes and the functional proteins related to osteoclasts. First, to test the ability of Ca-polyCpG MDNs to activate TLR9, Raw264.7 cells were transfected with an NF-κB reporter gene according to previous works (*51*, *52*). We observed NF-κB luciferase activity in cells after incubation with Ca-polyCpG MDNs or CpG to evaluate the ability of Ca-polyCpG MDNs to activate the TLR9. The results indicated that no luciferase activity was observed in cells treated with PBS controls. Luciferase activity was observed in cells incubated with Ca-polyCpG MDNs of CpG, demonstrating that Ca-

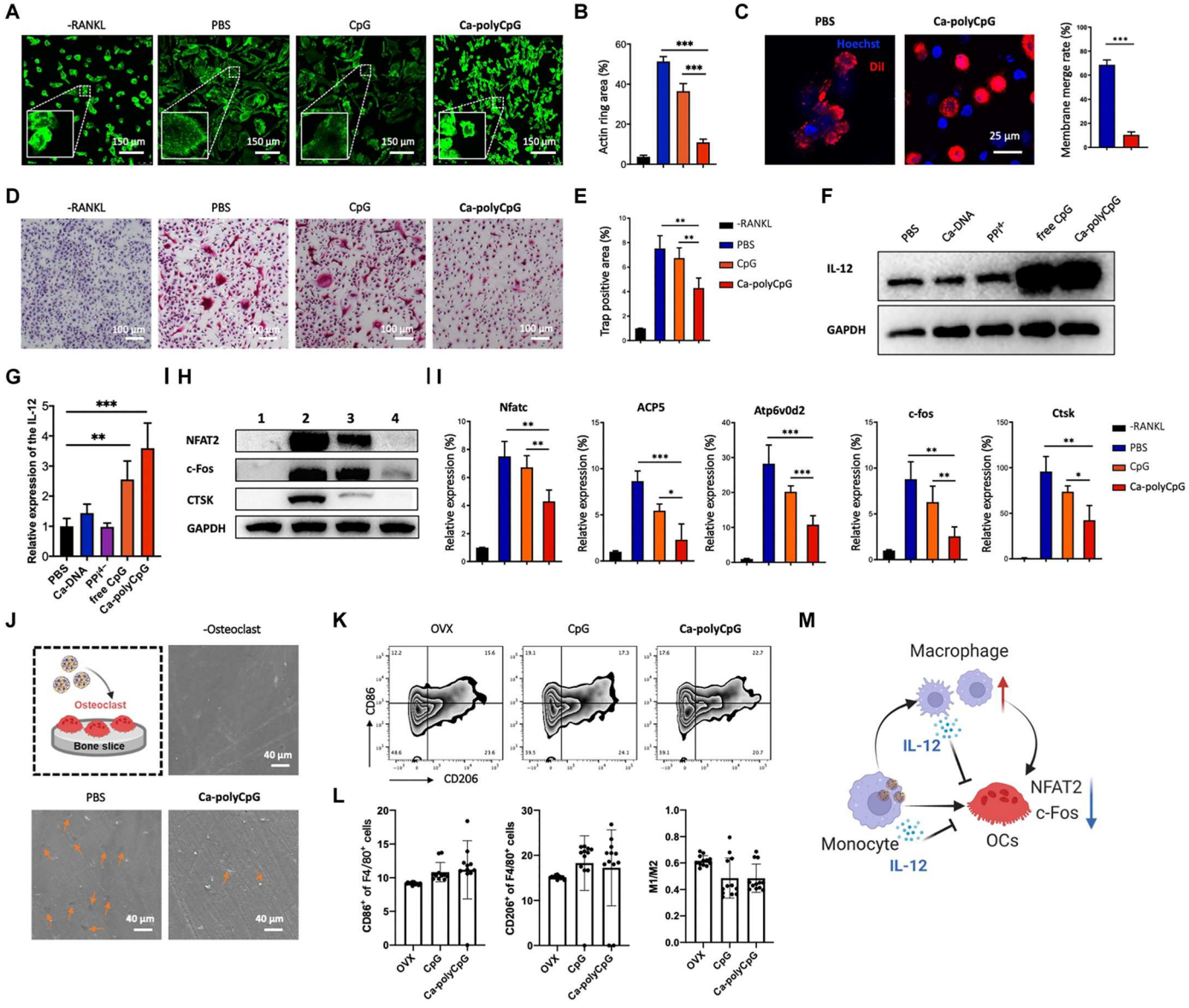

Fig. 3. Ca-polyCpG MDNs inhibit differentiation, activation, and bone resorption of osteoclast. (**A** and **B**) Representative images and quantitative analysis of BMM actin ring formation after treatment of PBS, CpG, and Ca-polyCpG MDNs. RANKL was added to induce the BMM differentiation into osteoclast. Cells were stained with actin (green) and Hoechst (blue). Scale bar, 150 μm. (**C**) Quantification analysis of the membrane merge rate of the BMMs after treatment of Ca-polyCpG MDNs. (**D** and **E**) Representative images and quantitative analysis of TRAP-positive cells treated with CpG and Ca-polyCpG MDNs. Scale bar, 100 μm. Western blot (**F**) and qPCR (**G**) analysis of IL-12 protein levels in BMMs after different treatments. The Western blot (**H**) and qPCR (**I**) assay showed that Ca-polyCpG MDNs could down-regulate osteoclast function effector proteins and genes. (**J**) The schematic diagram and SEM images showed the prevention of osteoclast acid erosion after treatment of Ca-polyCpG MDNs in the bone resorption assay. Scale bar, 40 μm. FACS (**K**) and quantitative (**L**) analysis of $CD86^+$ M1 and $CD206^+$ M2 macrophages in $F40/80^+$ and $CD11b^+$ gated tibial bone marrow cells from sham and OVX mouse after treatment of CpG or Ca-polyCpG MDNs. (**M**) The schematic diagram shows the mechanism of MDN inhibition of osteoclast formation. Data are presented as means ± SD. *P < 0.05, **P < 0.01, and ***P < 0.001.

polyCpG MDNs can efficiently activate TLR9 and CpG (fig. S14). At the same time, it was found that under the stimulation of Ca-polyCpG MDNs and CpG, monocytes secreted a large amount of IL-12, while Ca-DNA or PPi^{4-} had no effect on it (Fig. 3, F and G), indicating that polyCpG in Ca-polyCpG MDNs helps to induce the secretion of IL-12. Western blot and quantitative real-time polymerase chain reaction (RT-PCR) analyses were performed to determine the inhibitory impact of Ca-polyCpG MDNs on osteoclasts' activity. As shown in Fig. 3 (H and I), the expression of osteoclast function effector genes (e.g., c-fos, Atp6v0d2, Acp5, Ctsk, and Nfatc1) and corresponding proteins (e.g., NFATc1, c-Fos, and CTSK) was notably down-regulated after treatment of Ca-polyCpG MDNs. Compared to free CpG treatment, Ca-polyCpG MDNs showed a much better inhibitory effect on osteoclast differentiation due to the multivalent effect of polyCpG and enhanced cellular internalization ability.

Furthermore, we evaluated osteoclasts' capacity to resorb bone using a bovine bone resorption test as published previously (*53*, *54*). The surface of bovine bone was first plated with BMMs in the presence of RANKL, and then the inhibitory effect of Ca-polyCpG MDNs on osteoclasts-mediated bone resorption was evaluated. As shown in the SEM images, the PBS group showed obvious acidic etched bone defects, whereas the amount and area of bone resorption in the Ca-polyCpG MDN group were dramatically decreased (Fig. 3J). Together, Ca-polyCpG MDNs could greatly limit the differentiation and function of osteoclasts.

As the polarization state of macrophages in osteoporotic microenvironment was associated with osteoclast formation (*45*), we further investigated the influence of Ca-polyCpG MDNs on macrophage polarization in vivo using the OVX mice model, a typical animal model to study postmenopausal osteoporosis (*55*). After 1 month of removing the bilateral ovaries of C57BL/6J mice, the isolated uterus without ovaries had noticeable shrinkage, confirming the successful construction of the OVX mice model (figs. S15A and S16). To investigate the immunostimulatory effects of Ca-polyCpG MDNs on BMMs in vivo, OVX mice were administered with Ca-polyCpG MDNs or CpG for 4 days via a percutaneous mini-invasive injection, and the proportion of M1 and M2 phenotype in the bone marrow was analyzed by FACS. The results showed that Ca-polyCpG MDNs exhibited the most substantial inductive effects on macrophage polarization to M1 phenotype ($CD86^+$) in comparison with the free CpG and negative control (Fig. 3, K and L, and fig. S17). The M2 phenotype ($CD206^+$) was also increased, while the ratio of M1 to M2 was not notably increased. These results are consistent with previous studies showing that macrophages play a critical role in tissue repair and bone remodeling and that proinflammatory cytokines released by macrophages are essential for early fracture repair (*56*, *57*). On the other hand, although macrophages can differentiate into osteoclasts to some extent, monocytes are the most important precursor cells of osteoclasts. Therefore, reducing the numbers of monocytes may be beneficial in alleviating osteoporosis (*4*, *58*). For example, it has been reported that CpG can reduce the number of osteoclasts by inducing the activation of the TLR9 signaling pathway to steer BMM precursors toward M1 macrophage lineage rather than the osteoclast lineage (*24*). Not all M1 macrophages differentiate into osteoclasts; certain conditions, such as the presence of IL-4, are required for this differentiation process to occur (*59*, *60*).

Together, according to previous research and our experimental results, Ca-polyCpG can inhibit the differentiation of osteoclasts by stimulating the secretion of IL-12 from monocytes and reduce expression of osteoclast function effector protein (such as c-Fos and NFTA2). Although Ca-polyCpG can stimulate the enhancement of the number of M1 macrophages, there is no notable change in the ratio of M1/M2, which does not affect the changes of inflammation in the bone microenvironment. Since monocytes are the primary precursor cells for osteoclasts, reducing the numbers of monocytes may be beneficial in alleviating osteoporosis (Fig. 3M).

PPi^{4-}-mediated bone targeting enhances the retention of Ca-polyCpG MDNs in bone tissue

PPi^{4-}, as a bisphosphonate analog, has a strong affinity for bone tissue (*61*, *62*). The PPi^{4-} produced during the preparation of Ca-polyCpG MDNs may contribute to enhanced retention of Ca-polyCpG MDNs in bone tissue. In vitro studies involving coincubation of bone slices with Cy5-labeled Ca-polyCpG containingPPi^{4-} and Ca-DNA without PPi^{4-} for 24 hours revealed that Ca-polyCpG had a higher retention rate in bone tissue than Ca-DNA. These findings provided evidence that PPi^{4-} can enhance the retention of Ca-polyCpG in bone tissue (Fig. 4A). In further experiments, percutaneous mini-invasive injection of Cy5-labeled Ca-polyCpG MDNs into the left tibia was performed, and fluorescence was observed in the tibia within 24 hours (fig. S18). This observation confirmed that Ca-polyCpG can achieve long-term retention in osteoporotic bone.

To explore whether the enhanced bone retention of Ca-polyCpG MDNs could induce bone targeting in vivo, we used a systematic administration in OVX mice. A critical factor for successful in vivo tumor targeting is prolonged circulation time in the bloodstream. To investigate this, we performed an experiment to determine the circulation time of Cy5-modified Ca-polyCpG or Ca-DNA in mice. Our results showed that the first and second half-life of Ca-DNA were 0.13 ± 0.03 hours and 4.4 ± 0.7 hours, and those of Ca-polyCpG were 0.43 ± 0.07 hours and 4.9 ± 2.3 hours (fig. S19). Next, to evaluate the bone targeting ability of Ca-polyCpG, Cy5-labeled Ca-polyCpG with PPi^{4-} or Ca-DNA without PPi^{4-} was injected intravenously into mice, followed by detection of fluorescence intensity in bone tissue (spine and hindlimb) after 24 hours. The results showed that the fluorescence signal of Ca-polyCpG in bone tissue was significantly stronger than that of Ca-DNA without PPi^{4-}, indicating the bone affinity of PPi^{4-} and the apparent targeting and retention ability of Ca-polyCpG in osteoporotic bone (Fig. 4, B and C, and fig. S20). Together, with the prolonged circulation time and the high affinity of PPi^{4-} to bone tissue, Ca-polyCpG can achieve effective targeting to bone tissue and achieve long-term retention in osteoporotic bones.

Anti-osteoporosis efficacy of Ca-polyCpG MDNs in OVX mice and rabbits

Next, the anti-osteoporosis effect of Ca-polyCpG MDNs was studied in OVX mice by local administration. C57BL/6J mice were either OVX or sham-operated and then percutaneously injected with PBS or Ca-polyCpG MDNs (25 mg kg^{-1}) every week, for a total of three times (Fig. 4D). Two months after the surgery, micro-CT was used to investigate the protective effects of Ca-polyCpG MDNs on tibia bone. As illustrated in Fig. 4E and fig. S21, after treatment of Ca-polyCpG MDNs, the bone loss in bone tissues induced by the OVX procedure was inhibited, and osteopenic phenotypes in trabecular bones were alleviated. The quantitative measurement of bone characteristics revealed that BV/TV and Tb.N were significantly increased in the Ca-polyCpG MDN group compared with the PBS group, and both nearly returned to normal levels (Fig. 4G). As observed by hematoxylin and eosin (H&E) staining, compared to that in the PBS group, the bone volume and bone surface in the Ca-polyCpG MDN group were well maintained (Fig. 4F). To investigate osteoclast development, the sections of the tibia bone were TRAP stained. As shown in Fig. 4H, the OVX procedure led to an increased number of osteoclasts (TRAP-positive cells), whereas Ca-polyCpG MDN treatment dramatically inhibited osteoclast formation on tibia bone, decreasing it back to the normal level.

Next, the potential of Ca-polyCpG MDNs to enhance bone formation was evaluated by the calcine double-labeling experiment, which reflects the mineral apposition rate (MAR) (*63*, *64*). Relative

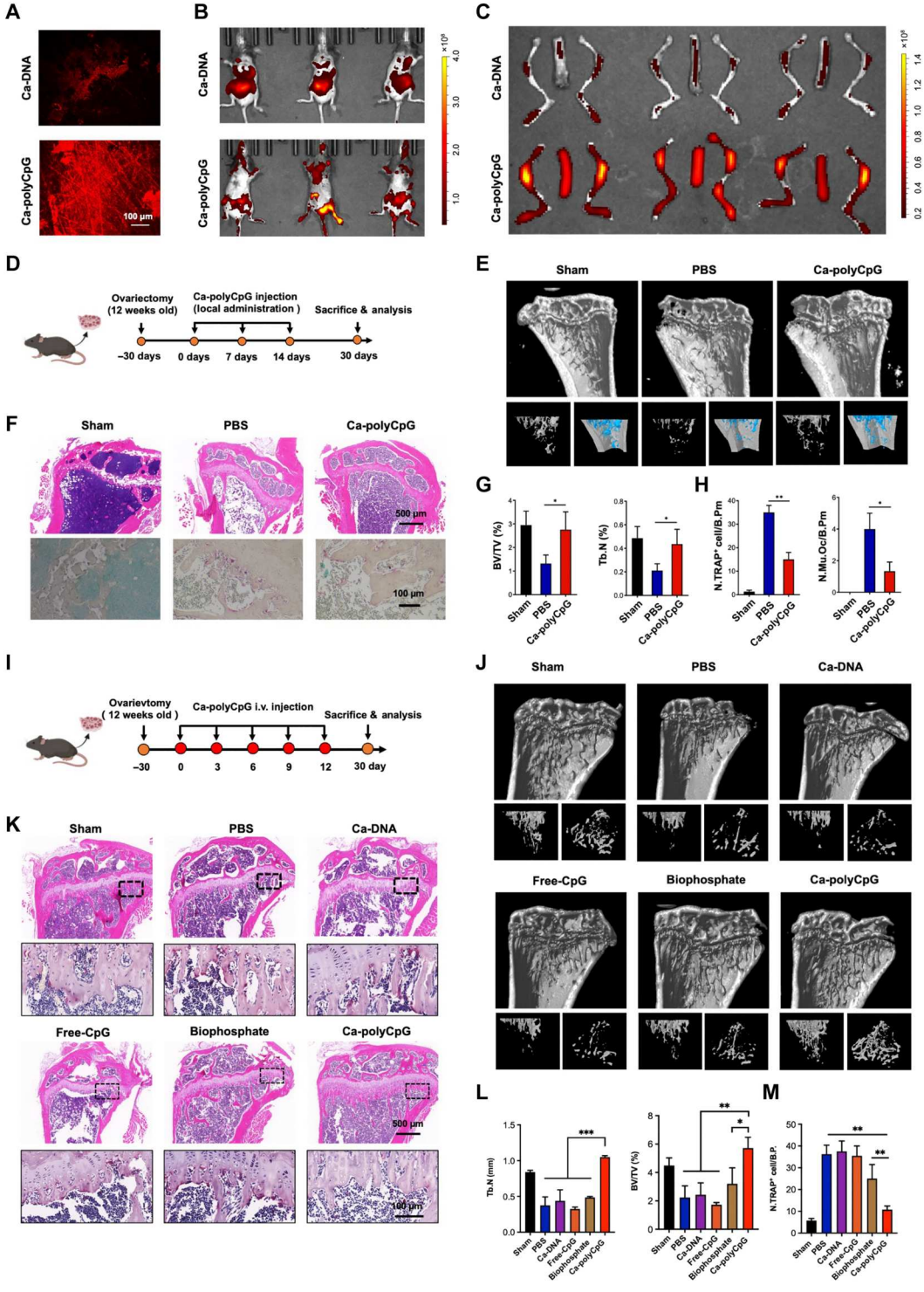

Fig. 4. Anti-osteoporotic efficacy of Ca-polyCpG MDNs in OVX mouse model. (**A**) Fluorescence microscopy imaging of Ca-polyCpG MDNs and Ca-DNA distribution on the surface of bone slices. In vivo (**B**) and bone tissue (spine and hindlimb) (**C**) fluorescence images showed the bone targeting of Ca-polyCpG MDNs compared to that without PPi^{4-} modified Ca-DNA at 24 hours. (**D**) Schematic illustration of the establishment of the OVX C57/BL6 mouse model and the experimental design to evaluate the protective effects of Ca-polyCpG MDNs against osteoporosis by local administration. (**E**) Representative micro-CT images of tibial bone after various treatments. (**F**) H&E- and TRAP-stained photomicrographs of tibial section collected from mice after various treatments. (**G**) BV/TV and Tb.N values of mouse tibial bone calculated from micro-CT images ($n = 4$). (**H**) Quantification analysis of $TRAP^+$ cells/bone surface ($N.TRAP^+$ cells/B.Pm) and multiple nuclear osteoclast numbers/bone surface (N.Mu.Oc/B.Pm) from mice after various treatments ($n = 4$). (**I**) Schematic illustration of the establishment of the OVX C57/BL6 mouse model and the experimental design to evaluate the protective effects of Ca-polyCpG MDNs against osteoporosis by intravenous (i.v.) injection. (**J**) Representative micro-CT images of tibial bone after various treatments. (**K**) H&E- and TRAP-stained photomicrographs of tibial section collected from mice after various treatments. (**L**) BV/TV and Tb.N values of mouse tibial bone calculated from micro-CT images ($n = 4$). (**M**) Quantification analysis of $TRAP^+$ cells/bone surface ($N.TRAP^+$ cells/B.Pm) from mice after various treatments ($n = 4$). Data are presented as means ± SD. $^*P < 0.05$, $^{**}P < 0.01$, and $^{***}P < 0.001$.

to the PBS group, the OVX mice treated with Ca-polyCpG MDNs showed increased bone formation in both the trabecular and cortical bone, observing the longer distance between the two green lines (fig. S22A). Quantitation of the MAR and bone formation rate per unit of bone surface (BFR/BS) further demonstrated that Ca-polyCpG MDNs could significantly enhance bone formation (fig. S22B). Last, the three-point bending tests were used to study the bone strength change against pressure after Ca-polyCpG MDN treatment (fig. S23A). As illustrated in figs. S23B and S24, the tibia bone from Ca-polyCpG MDN–treated OVX mice showed enhanced material strength and greater resistance to fractures compared to the PBS group.

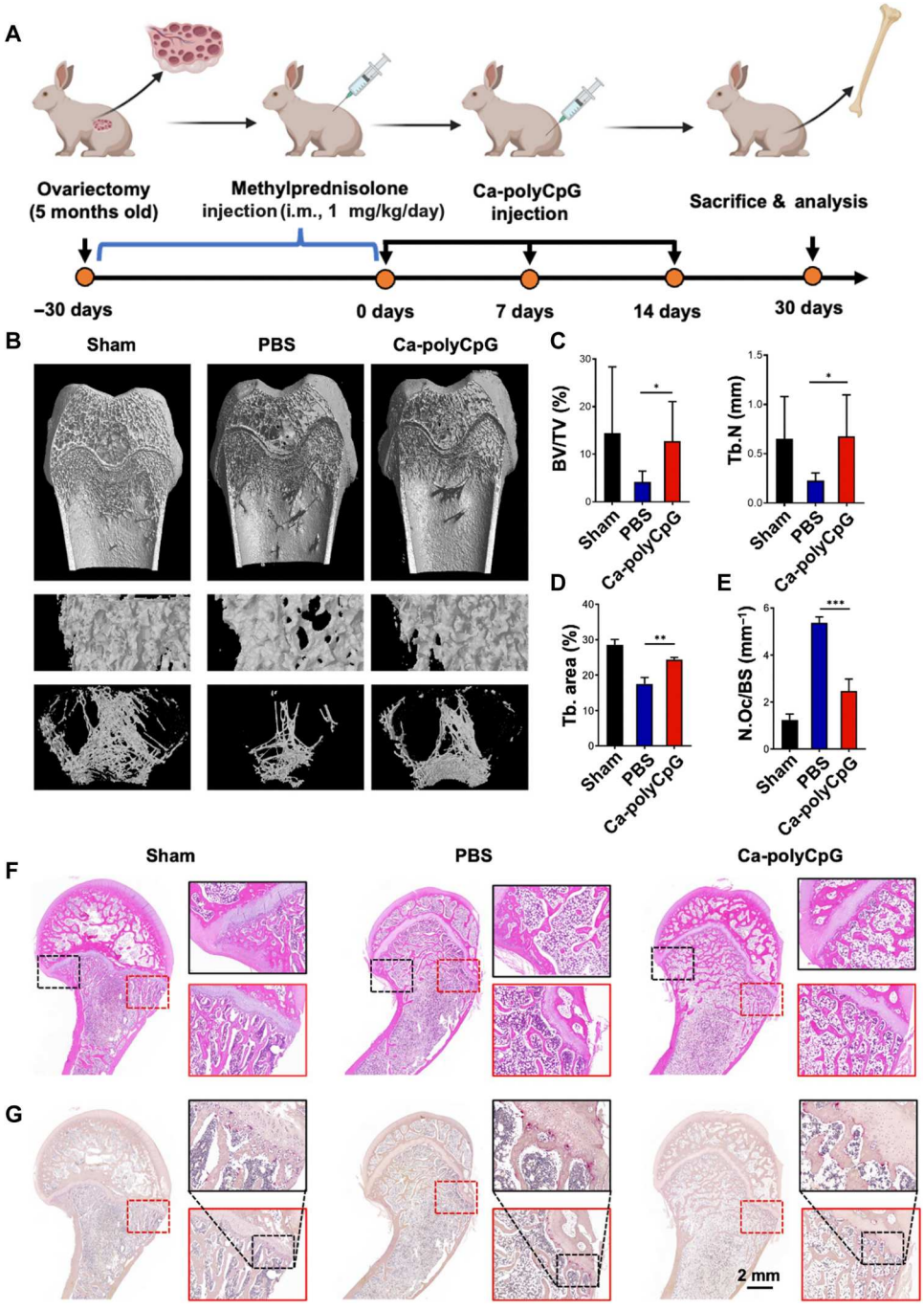

Fig. 5. Anti-osteoporosis efficacy of Ca-polyCpG MDNs in OVX rabbit model. (**A**) Schematic illustration of the establishment of the OVX rabbit model and the experimental design to evaluate the protective effects of Ca-polyCpG MDNs against osteoporosis. i.m., intramuscularly. (**B**) Representative micro-CT images of rabbit tibial bone from mice after various treatments. (**C**) BV/TV and Tb.N of rabbit tibial bone calculated from micro-CT images in (B) (n = 3). (**D**) Quantification analysis of Tb area/tissue area × 100% in (G). (**E**) The osteoclast numbers were calculated from (G). (**F** and **G**) Pathological and TRAP-stained observation of the tibial head from mice after various treatments at different magnifications. Data are presented as means ± SD. *P < 0.05, **P < 0.01, and ***P < 0.001.

Since age-related osteoporosis is a systemic disease and Ca-polyCpG MDNs have bone-targeting property, we also adopted systematic administration to study the effect of Ca-polyCpG MDNs on anti-osteoporosis treatment in vivo. To evaluate the efficacy of Ca-polyCpG MDNs in vivo, we compared their performance with that of clinical bisphosphonate drugs (zoledronic acid) and Ca-DNA assembled by Ca^{2+} and nonfunctional long ssDNA. C57BL/6J mice were subjected to either OVX or sham surgery and then intravenously injected with PBS, CpG, Ca-DNA, zoledronic acid, or Ca-polyCpG MDNs for a total of five times over a 3-day period (Fig. 4I). Two months after surgery, micro-CT was performed to evaluate the effect of treatment on OVX-induced bone loss. Our results showed

that Ca-polyCpG MDN treatment effectively inhibited bone loss in bone tissue and alleviated osteopenic phenotypes in trabecular bone compared to other groups (Fig. 4J). Quantitative measurements of bone characteristics showed that BV/TV and Tb.N were significantly increased in the Ca-polyCpG MDN group compared with the other groups and almost returned to normal levels (Fig. 4L). Histological examination by H&E staining revealed that bone volume and bone surface were well preserved in the Ca-polyCpG MDN group compared with the other groups (Fig. 4K). To investigate the effect of Ca-polyCpG MDN on osteoclast formation, tibial bone sections were stained for TRAP. The results showed that Ca-polyCpG MDN treatment dramatically inhibited osteoclast formation on the tibia bone and returned it to normal levels (Fig. 4M). Overall, our results suggest that Ca-polyCpG MDNs hold promise as a potential anti-osteoporosis treatment because they effectively target bone tissue and demonstrate superior efficacy compared to other treatments tested in this study.

Anti-osteoporosis efficacy of Ca-polyCpG MDNs in OVX rabbits

In addition to the OVX mice model, the therapeutic efficacy of Ca-polyCpG MDNs on osteoporosis was also evaluated in the OVX rabbit model. The OVX rabbit model was obtained by receiving an intraperitoneal injection of hyperthyroidism (1 mg/kg) daily for 8 weeks after OVX surgery (Fig. 5A and fig. S15B). One month after the surgery, the OVX rabbits were injected with Ca-polyCpG MDNs by a percutaneous mini-invasive injection weekly for a total of three times. Another month later, the rabbits were sacrificed, and the tibia bone was removed for micro-CT imaging, H&E staining, and TRAP staining analysis (Fig. 5A). As shown in micro-CT imaging, compared to that in the PBS group, the trabecular structures in the Ca-polyCpG MDN group were more robust and thicker, thus showing a narrower separation of trabecular (Fig. 5B). BV/TV and Tb.N of the Ca-polyCpG MDN group were also significantly increased in comparison to that in the PBS group (Fig. 5C).

As observed by H&E staining images, Ca-polyCpG MDNs efficiently decreased the degree of trabecular bone erosion by osteoclasts. In addition, the bone volume and bone surface of the tibia bone were both well maintained after treatment with Ca-polyCpG MDNs (Fig. 5F). The analysis of the TRAP staining (Fig. 5, E and G) illustrated that multinuclear $TRAP^+$ osteoclasts on the trabecular bone in the Ca-polyCpG MDN group were almost back to the normal level. Together, these results demonstrated that Ca-polyCpG MDNs are an optimal therapeutic candidate for preventing osteoporosis by inhibiting pathological osteoclasts and promoting bone repair in vivo.

Last, the biosafety of Ca-polyCpG MDN administration was evaluated. It is worth mentioning that no adverse events or fatalities were reported after the OVX procedure and Ca-polyCpG MDN administration via a percutaneous mini-invasive injection (fig. S25). Complete blood panel and blood biochemistry analysis of mice after Ca-polyCpG MDN treatment suggest the good tolerance of the therapy within 30 days after intravenous injection of Ca-polyCpG MDNs at the dose given in healthy mice (fig. S26). H&E staining of major organs also exhibited no obvious histological toxicity within 30 days after intravenous injection of Ca-polyCpG MDNs (fig. S27) in healthy mice, exhibiting relatively good tolerance of the Ca-polyCpG MDN formulation.

DISCUSSION

Osteoporosis is a bone disease characterized by an abnormal bone microenvironment involving multiple cell types, inorganic components, physicochemical properties, and signaling molecules. The complexity of this disease makes it difficult to treat with traditional single-function materials. In this study, we present a novel approach to treat osteoporosis using metal-polyDNA frameworks (MDNs) coordinated with calcium ions and a long ssDNA (Ca-polyCpG MDNs) to reconstruct the osteoporotic microenvironment.

Our Ca-polyCpG MDNs were designed to effectively reconstruct the bone microenvironment and treat osteoporosis in several ways. First, Ca-polyCpG MDNs have the ability to neutralize acid, which can counteract the erosion of bone tissue caused by mature osteoclasts (Fig. 2). Second, Ca-polyCpG MDNs can provide calcium supplementation and improve bone mineralization. This is also shown in Fig. 2, which illustrates the increased calcium deposition in bone tissue treated with Ca-polyCpG. Third, the CpG component of Ca-polyCpG can induce the secretion of IL-12 and reduce the expression of function-related proteins (such as NFTA2 and c-Fos) in osteoclasts, thus inhibiting the generation of osteoclasts (Fig. 3). In addition, Ca-polyCpG MDNs have the ability to regulate the differentiation of monocytes, macrophages, and osteoclasts. Besides, mediated by the RCA product PPi^{4-}, Ca-polyCpG can achieve targeting and retention of bone tissue (Fig. 4). Furthermore, in vivo anti-osteoporosis experiments demonstrated that Ca-polyCpG MDNs showed superior anti-osteoporosis efficacy compared to free CpG, Ca-DNA, and bisphosphonate, which are single-function materials (Fig. 4). Overall, the multifunctional Ca-polyCpG MDNs can effectively reconstruct the osteoporotic microenvironment, thereby improving the treatment of osteoporosis.

MATERIALS AND METHODS

Materials, cell, and animal

Calcium chloride [$CaCl_2$; Analytical reagent (AR), >99%], ammonium sulfate [$(NH_4)_2SO_4$; AR, 99%], 1,4-dithio-DL-threitol (DTT; biotechnology grade, 99.5%), CCK-8, Hoechst 33342, Dulbecco's modified Eagle's medium (DMEM), α-minimum essential medium (α-MEM), fetal bovine serum (FBS), penicillin, streptomycin, trypsin, and chemicals for TRAP stain were obtained from Sigma-Aldrich (St. Louis, USA). Recombinant mouse M-CSF and mouse RANKL were obtained from R&D Systems (Minneapolis, MN, USA). T4 DNA ligase (20,000 U) and phi29 DNA polymerase (1250 U) were purchased from Beyotime Institute of Biotechnology (Shanghai, China). DNA size markers and deoxynucleoside triphosphates (dNTPs) were purchased from Tiangen Biotech Co. Ltd. (Beijing, China). All related DNA sequences (table S1) and primers for quantitative PCR (qPCR) were synthesized and purified by Beijing Hippo Biotechnology Co. Ltd. (Beijing, China). Phycoerythrin (PE)–CD86, peridinin chlorophyll protein (PerCP)–CD11b, allophycocyanin (APC)–CD206, and FITC-F4/80 antibody for FACS analysis were purchased from Invitrogen eBioscience (Thermo Fisher Scientific). Specific antibodies against F4/80 and inducible nitric oxide synthase (iNOS) for immunofluorescence were from Abcam (Cambridge, UK). Specific primary antibodies against NFAT2, c-Fos, CTST, CTSK, and glyceraldehyde-3-phosphate dehydrogenase (GAPDH) for Western blotting assay were from Cell Signaling Technology (Danvers, MA, USA).

Raw264.7 cells were grown in DMEM supplemented with 10% FBS and 1% penicillin-streptomycin in high glucose and screened with puromycin. BMMs were isolated from 6- to 8-week-old C57BL/6J mice as previously reported (*5*). The bone marrow was flushed from femur and tibia bone and then cultured in α-modified minimal complete medium containing 10% FBS and penicillin plus streptomycin. To obtain pure BMMs, adnexal-free cells were collected and cultured in complete α-MEM plus M-CSF (25 ng/ml). After 3 days of culture, the attached cells were used for subsequent experiments.

C57BL/6J mice (female, age 6 to 7 weeks) were obtained from Shanghai Laboratory Animal Center (China). New Zealand rabbits (female, age 5 to 6 months) were obtained from Shanghai Legend Biotechnology Co. Ltd. All animal experiments were performed under the guidelines evaluated and approved by the ethics committee of Institutional Animal Care and Use Committee of Shanghai Jiao Tong University.

Preparation and characterization of Ca-polyCpG

PolyCpG was synthesized using RCA. First, to connect templates and primers, 100 μM of linear 5′-phosphorylated DNA template containing CpG coded sequence and 200 μM primary primer were mixed with a ratio of 1:2 in PBS solution. Then, the mixture was heated at 95°C for 2 min and gradually cooled to 20°C at a rate of 1°C/min using a PCR thermal cycler to prepare the circ-DNA template. After annealing, T4 DNA ligase (2 U μl^{-1}) was added and then incubated at 16°C overnight. After that, the solution was heated to 65°C for 10 min to inactivate the T4 DNA ligase.

In the amplification process, the circ-DNA template (0.5 μM), dNTPs (1 mM), and phi29 DNA polymerase were added sequentially into the 50 μl RCA reaction buffer containing 50 mM tris-HCl, 10 mM $(NH_4)_2SO_4$, 50 mM KCl, 4 mM DTT, and 10 mM $MgCl_2$. Then, the mixture was incubated at 30°C for 2 hours. The reaction was terminated after heating at 65°C for 10 min to inactive phi29 DNA polymerase. To label the repetitive CpG sequence, a Cy5-labeled CpG complementary sequence (Cy5-CpG_{beacon}) was added to the reaction system. To coordinate with calcium ions, 20 mM $CaCl_2$ was added in the reaction system and incubated for 12 hours at 4°C. The prepared Ca-polyCpG MDNs were centrifuged at 10,000 rpm for 5 min and washed three times with water. The DNA concentrations were analyzed with a NanoDrop photometer during the process of the RCA, according to previous report (*65*).

To verify the success of polyCpG synthesis, primers, templates, circular DNA templates, and final Ca-polyCpG from the RCA procedure were performed in a 2% natural agarose gel at 120 V with tris-acetate-Ethylene Diamine Tetraacetic Acid (EDTA) for 1 hour. The gels were scanned with the ChemiDoc MP Imaging System (Bio-Rad Laboratories, USA).

The hydrodynamic diameters of Ca-polyCpG MDNs were examined by DLS using the ZetaSizer NanoZS instrument (Malvern, Worcestershire, UK). The shape and structure of Ca-polyCpG MDNs were characterized using TEM (je -2100, Tokyo, Japan) and SEM (TM-1000, Hitachi, Tokyo, Japan).

pH-triggered Ca^{2+} release of Ca-polyCpG MDNs

One hundred microliters of Ca-polyCpG MDNs was added to 400 μl of PBS buffer at pH 7.4 and 5.0. After incubation at 37°C for various times (0.5, 1, 2, 4, 8, and 12 hours), the released calcium ions were collected through an ultrafiltration tube (Millipore, 0.5 ml, 30 kDa) and then determined by colorimetric assay (colorimetric method, Abcam). The morphology of Ca-polyCpG MDNs after treatment with different pH buffers was observed by TEM (JEM-2100, Tokyo, Japan).

Neutralization titration experiment

Ca-polyCpG MDNs (5 mg/kg) were titrated with 0.5% hydrochloric acid (20 μl per titration) under magnetic stirring. The pH was continuously monitored by a pH meter. The titration was stopped when the three consecutive pH decreases were less than two.

Acid neutralization assay of Ca-polyCpG MDNs

To evaluate the extracellular acid state of the bone slice surface with osteoclasts after Ca-polyCpG MDN treatment, we immersed the bone slices in the FITC, which can be visualized as green fluorescence at an excitation wavelength of 488 nm, and incubated them with PBS, Ca-DNA, PPi^{4-}, free CpG, or Ca-polyCpG MDN solution mentioned above. The mature osteoclasts were seeded onto the surface of the bone slices treated with PBS, Ca-DNA, PPi^{4-}, free CpG, or Ca-polyCpG MDNs. The samples were then fixed with 4% paraformaldehyde (PFA) and stained with DiI and DAPI. The images were captured and analyzed through a confocal laser scanning microscope (LCM). To calculate the pH within the acidic environment of the osteoclast, FITC on the surface of the bone section was used as a pH probe, and the fluorescence intensity of FITC in acidic milieu was detected by LCM.

In vitro recovery of osteoporotic bone

In vitro assay of the bone mineralization properties of Ca-polyCpG MDNs were detected in cell-free osteoporotic bone. (i) PBS, (ii) $CaCl_2$, (iii) Ca-DNA (no PPi^{4-}), (iv) Ca-polyCpG MDNs, and (v) acid-treated Ca-polyCpG MDNs were injected into the osteoporotic bones, and then the bones were placed in a water bath at 37°C for 14 days. After drying at room temperature, a high-resolution micro-CT (Skyscan1176, Bruker, USA) was used to analyze the tibia, operating at a voltage of 80 kV and a current of 80 μA. The auxiliary software of the micro-CT scanner was used to perform three-dimensional (3D) reconstruction from the sequential scans. Quantitative results of the micro-CT analysis were measured using the CTAn program. STEM (TM-1000, Hitachi, Tokyo, Japan) was used to observe the content of calcium and phosphorus in osteoporotic bones.

Cellular uptake and cytotoxicity assay of Ca-polyCpG MDNs

Raw264.7 macrophages were seeded into 96-well plates (1×10^4 cells per well) and incubated overnight to assay the cytotoxicity. Different concentrations of Ca-polyCpG MDNs were added to the plates for another 48 hours of incubation. Next, CCK-8 was used to measure the cell activity according to the manufacturer's instructions. Cytotoxicity after the same treatments was also examined using calcein-AM/PI dual-staining assay.

Raw264.7 macrophage cells were seeded into 24-well plates (5×10^4 cells per well) and incubated overnight. For cellular uptake, after being incubated with 50 nM Cy5-labeled Ca-polyCpG MDNs or Cy5-CpG for 4 hours, the cells were fixed in 4% PFA, stained with Hoechst, and observed with a confocal laser scanning microscope (TCS SP8, Leica, Germany). For the measurement of the uptake by flow cytometer, the Raw264.7 macrophage cells were seeded in six-well culture plates (1×10^5 cells per well) overnight

and incubated with different concentrations of the 50 nM Cy5-labeled Ca-polyCpG MDNs or Cy5-CpG for 4 hours, followed by flow cytometry assay. FACS analysis was conducted with the FACS-Calibur Flow Cytometer (BD Biosciences, Franklin Lakes, NJ, USA).

In vitro osteoclastogenesis assay

BMMs were gently seeded into the 24-well plates (1×10^5 cells per well) containing the dish and further stimulated with M-CSF (30 ng ml^{-1}) and RANKL (100 ng ml^{-1}). The medium was replaced every 2 days, and equivalent M-CSF and RANKL were added until osteoclasts formed. The Ca-polyCpG MDNs and CpG (50 nM) were added at day 2. After 5 days, the cells were washed and fixed with 4% PFA for 15 min at room temperature. Then, TRAP enzymatic activity was evaluated with an acid phosphatase leukocyte kit according to the manufacturer′s instructions. The cell′s contour profile and podosome belt formation were labeled with phalloidin (Thermo Fisher Scientific). Cells were imaged with a confocal laser scanning microscope (TCS SP8, Leica, Germany).

In vitro assay for osteoclast fusion

BMMs were gently seeded into the 24-well plates (1×10^5 cells per well) containing the dish. After 3 days of incubation with M-CSF (30 ng ml^{-1}) and RANKL (100 ng ml^{-1}), cells were labeled with the blue fluorescent nuclear dye Hoechst or red fluorescent cell membrane dye Dil at room temperature. The two groups of cells were cocultured on the plate and treated with Ca-polyCpG MDNs (50 nM) for 24 hours. Next, a confocal laser scanning microscope (TCS SP8, Leica, Germany) was used to observe osteoclast fusion. The membrane merge rate was determined using ImageJ as described previously (*66*).

Bone slice resorption assay

BMMs were plated on the surface of the freeze-dried beef bone slices in complete α-MEM with M-CSF (30 ng ml^{-1}) at a density of 2×10^5 cells per well to simulate the in vivo bone resorption effect. RANKL (50 ng ml^{-1}) was used to stimulate cell osteoclastogenesis for 5 days. Then, Ca-polyCpG MDNs (50 nM) were added in the solution during the stimulation. Next, the bone slices were fixed with 4% PFA for 30 min, and the surface cells on the bone slices were scraped off with a brush. The bone slices were sputter-coated with Au-Pd and observed by SEM (TM-1000, Hitachi, Tokyo, Japan) as previously described (*53*).

qPCR and Western blotting assay

BMMs were treated with and without RANKL and cultured for 5 days on six-well plates in the presence of CpG or Ca-polyCpG MDNs (50 nM). Total RNA was isolated from cells using an RNA kit (Qiagen, Valencia, CA, USA). RNA was transcribed to cDNA using HiScript III RT SuperMix (Vazyme, Piscataway, NJ, USA). RT-qPCR system (LightCycler 480 II, Roche, USA) was used to perform the PCR procedure according to the manufacturer′s instructions. The primers used for PCR were as follows: IL-12, 5′-ATGCAGCAAGTGGGCATGTGTT-3′ (forward) and 5′-TGCTTTCTTTCAGGGACAGCCT-3′ (reverse); Nfatc1, 5′-TCCACCCACTTCTGACTTCC-3′ (forward) and 5′-CTTCGCCCACTGATACGAG-3′ (reverse); Acp5, 5′-CCATTGTTAGCCACATACGG-3′ (forward) and 5′-CACTCAGCACATAGCCCACA-3′ (reverse); c-fos, 5′-GTTCGTGAAACACACCAGGC-3′ (forward) and 5′-GGCCTTGACTCACATGCTCT-3′ (reverse); Ctsk, 5′-TCCGCAATCCTTACCGAATA-3′ (forward) and 5′-AACTTGAACACCCACATCCTG-3′ (reverse); Atp6v0d2, 5′-CAAAGCCAGCCTCCTAACTC-3′ (forward) and 5′-GTTGCCATAGTCCGTGGTC-3′ (reverse); β-actin, 5′-ACAGCAGTTGGTTGGAGCAA-3′ (forward) and 5′-ACGCGACCATCCTCCTCTTA-3′ (reverse), which was used as a reference gene to normalize the osteoblast-related genes.

Western blotting was performed to measure the protein expression of IL-12, NFAT2, c-Fos, CTSK, and GAPDH. BMMs were cultivated in six-well plates with CpG or Ca-polyCpG MDNs (50 nM) for 5 days with and without RANKL stimulation. To collect the proteins, the cells were lysed in a radioimmunoprecipitation lysis buffer. The extracted proteins were then separated using SDS–polyacrylamide gel electrophoresis. Poly(vinylidene difluoride) membranes were used for protein transfer after electrophoresis. After being blocked by nonfat milk, the membranes were incubated with primary antibodies with gentle shaking overnight. Then, the membranes were washed and incubated with horseradish peroxidase–conjugated secondary antibodies at room temperature for 1 hour. The chemiluminescence signals of the antibodies were detected with an enhanced chemiluminescence substrate (Thermo Fisher Scientific). Images were observed with the ChemiDoc MP Imaging System (Bio-Rad Laboratories, USA).

In vivo study of macrophage polarization

For in vivo study, C57BL/6J mice were either sham- or OVX-operated and then administrated by a percutaneous mini-invasive injection with either Ca-polyCpG MDNs (25 mg/kg) or PBS solution. Four days later, mice were sacrificed, and bone marrow macrophages were harvested from the tibia marrow flushing. Extracted bone marrow macrophages were stained for anti-CD86–PE, anti-CD206–APC, anti-CD11b–PerCP, and anti-F4/80–FITC and then processed for FACS analysis. CD86-positive macrophage population was assessed following gating of cells for F4/80 and CD11b (selection criteria for macrophages). The bone slides were rehydrated, and the antigen was retrieved by phosphate buffer solution for immunofluorescence detection of iNOS and F4/80. Bone slices were incubated in TBST solution (tris-buffered saline–Tween) containing 5% bovine serum albumin to inhibit nonspecific antigens. The sections were then treated overnight at 4°C with primary antibodies. The next day, bone slices were then washed and incubated in the dark for 1 hour with secondary antibody at 4°C. After counterstaining the nuclei by DAPI, bone slices were cleaned and placed on glass slides for confocal laser scanning microscopy (TCS SP8, Leica, Germany) assay.

OVX-induced osteoporosis mouse model

Fifteen C57BL/6J mice (females, 8 weeks old) were randomly divided into three groups: sham group (n = 5), OVX group (n = 5), and OVX plus Ca-polyCpG MDN group (25 mg kg^{-1}) group (n = 5). The osteoporosis model was established by performing the bilateral OVX under chloral hydrate anesthesia for the mice in the OVX group and OVX plus Ca-polyCpG MDN group. The sham procedure in which the ovaries were only exteriorized but not resected was prepared for the mice in the sham group. At 1 month of recovery following the operation, the mice in the OVX plus Ca-polyCpG MDNs were injected with Ca-polyCpG MDNs

through a percutaneous mini-invasive injection at 25 mg kg^{-1} every week for three times. The mice in the sham and OVX groups were injected with PBS as a control. All the mice were humanely sacrificed after 4 weeks of administration to evaluate the bone protection effect of Ca-polyCpG MDNs.

OVX-induced osteoporosis rabbit model

Nine New Zealand rabbits (females, 5 months old) were randomly divided into three groups: sham group ($n = 3$), OVX group ($n = 3$), and OVX plus Ca-polyCpG MDNs (25 mg/kg) group ($n = 3$). The osteoporosis rabbit model was established by performing the bilateral OVX under anesthesia, followed by receiving an intraperitoneal injection of hyperthyroidism (1 mg kg^{-1}) daily for 8 weeks after OVX surgery. The sham procedure, in which the ovaries were only exteriorized but not resected, was prepared for the rabbit in the sham group. After 1 month of the OVX surgery, the rabbits in the OVX plus Ca-polyCpG MDNs were injected with Ca-polyCpG MDNs by a percutaneous mini-invasive injection at 25 mg kg^{-1} every week for three times every week. The rabbits in the sham and OVX groups were injected with PBS as a control. All the rabbits were humanely sacrificed after 4 weeks of intravenous administration to evaluate the bone protection effect of Ca-polyCpG MDNs.

Micro-CT scanning and analysis

After sacrificing the mice, tibia bone tissues were collected and fixed in 4% PFA for 24 hours. Then, the tibias were analyzed by micro-CT (Skyscan1176, Bruker, USA) with the following parameter settings: a resolution of 8 m per pixel, a voltage of 80 kV, and a current of 124 A. The 3D models were analyzed by CTAox and CTVol. The trabecular bone of the bone marrow was analyzed for BV/TV, Tb.N, and Tb.Sp using CTAn program (Bruker micro-CT, Kontich, Belgium).

Bone histological evaluations

After micro-CT analysis, tibia bone tissues were harvested, fixed in 10% buffered formalin, and then incubated in decalcifying solution (14% EDTA) at room temperature for more than 1 month for decalcification. Then, the tibia bones were embedded in paraffin and cross-sectioned at 8 m in thickness. TRAP activity staining and H&E staining were used to evaluate the osteoclast and trabecular bone distribution in vivo. The number of osteoclasts per bone surface was calculated (*67*).

Calcein double staining

Calcein double staining method was used to detect bone formation activity in mice. Briefly, mice were injected with calcein (15 mg/kg, Sigma-Aldrich) 8 and 2 days before euthanasia. After being fixed in 4% PFA solution for 24 hours, the tibia bone collected from mice was sectioned using a hard tissue sectioning and grinding system at 20 μm thickness. Sections were imaged with a confocal laser scanning microscope (TCS SP8, Leica, Germany) and analyzed for periosteal bone and trabecular bone. Bone dynamic histomorphometric analyses for MAR and BFR/BS were determined by Bioquant Osteo software (v.7.20.10, Bioquant Nashville) (*68*).

Three-point bending test

The tibia of mice in the sham group, OVX group, and OVX plus Ca-polyCpG MDN group were collected and subjected to a three-point bending test with an electronic universal testing machine (HENGYI, HY-0230). The tibia with the physiological bending surface facing upward was fixed on a holder with two fixed loading points. At the midpoint of the two loading points, a 1.0-mm-thick steel plate perpendicular to the long axis of the tibia was used to apply a stable preload of 1 N. The bending load was applied at a constant displacement rate of 5 mm min^{-1} until a fracture occurred. The ultimate force, stiffness, and maximum energy absorption of the specimen were determined from the load-deflection bending curve.

Biocompatibility evaluation

Ca-polyCpG MDNs (25 mg kg^{-1}) were intravenously injected to healthy female C57BL/6J mice. Retro-orbital blood and major organs (heart, liver, spleen, lung, and kidney) were then collected from three mice per group at different time points. The major organs were fixed in 10% buffered formalin, embedded in paraffin, cross-sectioned at 8 μm in thickness, stained with H&E, and observed by overall perspective optical microscopy. Serum biochemistry assay and complete blood panel analysis were determined in Drug Safety Evaluation Research Center (Shanghai Institute of Materia Medica, Shanghai, China).

Statistical analysis

Statistical analysis was conducted using GraphPad Prism 9.0 software (La Jolla CA). All data were presented as means ± SD, and statistical analysis was performed using Student's t test. Differences between the two groups were determined to be significant at $^{*}P < 0.05$ and very significant at $^{**}P < 0.01$ and $^{***}P < 0.001$.

Supplementary Materials

This PDF file includes:

Table S1

Figs. S1 to S27

REFERENCES AND NOTES

1. J. M. Lane, L. Russell, S. N. Khan, Osteoporosis. *Clin. Orthop. Relat. Res.* **372**, 139–150 (2000).
2. B. Yu, C. Y. Wang, Osteoporosis: The result of an 'aged' bone microenvironment. *Trends Mol. Med.* **22**, 641–644 (2016).
3. A. Salhotra, H. N. Shah, B. Levi, M. T. Longaker, Mechanisms of bone development and repair. *Nat. Rev. Mol. Cell Biol.* **21**, 696–711 (2020).
4. J. Munoz, N. S. Akhavan, A. P. Mullins, B. H. Arjmandi, Macrophage polarization and osteoporosis: A review. *Nutrients* **12**, 2999 (2020).
5. X. Li, L. Wang, B. Huang, Y. Gu, Y. Luo, X. Zhi, Y. Hu, H. Zhang, Z. Gu, J. Cui, L. Cao, J. Guo, Y. Wang, Q. Zhou, H. Jiang, C. Fang, W. Weng, X. Chen, X. Chen, J. Su, Targeting actin-bundling protein L-plastin as an anabolic therapy for bone loss. *Sci. Adv.* **6**, eabb7135 (2020).
6. J. Luo, Z. Yang, Y. Ma, Z. Yue, H. Lin, G. Qu, J. Huang, W. Dai, C. Li, C. Zheng, L. Xu, H. Chen, J. Wang, D. Li, S. Siwko, J. M. Penninger, G. Ning, J. Xiao, M. Liu, LGR4 is a receptor for RANKL and negatively regulates osteoclast differentiation and bone resorption. *Nat. Med.* **22**, 539–546 (2016).
7. P. Chotiyarnwong, E. V. McCloskey, Pathogenesis of glucocorticoid-induced osteoporosis and options for treatment. *Nat. Rev. Endocrinol.* **16**, 437–447 (2020).
8. A. K. Nair, A. Gautieri, S. W. Chang, M. J. Buehler, Molecular mechanics of mineralized collagen fibrils in bone. *Nat. Commun.* **4**, 1724 (2013).
9. H. Fonseca, D. Moreira-Gonçalves, H. J. Coriolano, J. A. Duarte, Bone quality: The determinants of bone strength and fragility. *Sports Med.* **44**, 37–53 (2014).
10. Y. Li, G. Toraldo, A. Li, X. Yang, H. Zhang, W. P. Qian, M. N. Weitzmann, B cells and T cells are critical for the preservation of bone homeostasis and attainment of peak bone mass in vivo. *Blood* **109**, 3839–3848 (2007).
11. J. Tuckermann, R. H. Adams, The endothelium-bone axis in development, homeostasis and bone and joint disease. *Nat. Rev. Rheumatol.* **17**, 608–620 (2021).

12. M. N. Michalski, L. K. McCauley, Macrophages and skeletal health. *Pharmacol. Ther.* **174**, 43–54 (2017).
13. J. S. Chen, P. N. Sambrook, Antiresorptive therapies for osteoporosis: A clinical overview. *Nat. Rev. Endocrinol.* **8**, 81–91 (2011).
14. S. Khosla, L. C. Hofbauer, Osteoporosis treatment: Recent developments and ongoing challenges. *Lancet Diabetes Endocrinol.* **5**, 898–907 (2017).
15. Y. Zeng, J. Hoque, S. Varghese, Biomaterial-assisted local and systemic delivery of bioactive agents for bone repair. *Acta Biomater.* **93**, 152–168 (2019).
16. P. Yu, Y. Liu, J. Xie, J. Li, Spatiotemporally controlled calcitonin delivery: Long-term and targeted therapy of skeletal diseases. *J. Control. Release* **338**, 486–504 (2021).
17. L. Xue, N. Gong, S. J. Shepherd, X. Xiong, X. Liao, X. Han, G. Zhao, C. Song, X. Huang, H. Zhang, M. S. Padilla, J. Qin, Y. Shi, M. G. Alameh, D. J. Pochan, K. Wang, F. Long, D. Weissman, M. J. Mitchell, Rational design of bisphosphonate lipid-like materials for mRNA delivery to the bone microenvironment. *J. Am. Chem. Soc.* **144**, 9926–9937 (2022).
18. X. Lin, Q. Wang, C. Gu, M. Li, K. Chen, P. Chen, Z. Tang, X. Liu, H. Pan, Z. Liu, R. Tang, S. Fan, Smart nanosacrificial layer on the bone surface prevents osteoporosis through acid-base neutralization regulated biocascade effects. *J. Am. Chem. Soc.* **142**, 17543–17556 (2020).
19. Y. Zhou, Y. Deng, Z. Liu, M. Yin, M. Hou, Z. Zhao, X. Zhou, L. Yin, Cytokine-scavenging nanodecoys reconstruct osteoclast/osteoblast balance toward the treatment of post-menopausal osteoporosis. *Sci. Adv.* **7**, eabl6432 (2021).
20. W. Wang, Y. Xiong, R. Zhao, X. Li, W. Jia, A novel hierarchical biofunctionalized 3D-printed porous Ti6Al4V scaffold with enhanced osteoporotic osseointegration through osteoimmunomodulation. *J. Nanobiotechnol.* **20**, 68 (2022).
21. S. Yao, X. Lin, Y. Xu, Y. Chen, P. Qiu, C. Shao, B. Jin, Z. Mu, N. Sommerdijk, R. Tang, Osteoporotic bone recovery by a highly bone-inductive calcium phosphate polymer-induced liquid-precursor. *Adv. Sci.* **6**, 1900683 (2019).
22. H. D. Kim, H. L. Jang, H. Y. Ahn, H. K. Lee, J. Park, E. S. Lee, E. A. Lee, Y. H. Jeong, D. G. Kim, K. T. Nam, N. S. Hwang, Biomimetic whitlockite inorganic nanoparticles-mediated in situ remodeling and rapid bone regeneration. *Biomaterials* **112**, 31–43 (2017).
23. P. Mora-Raimundo, D. Lozano, M. Manzano, M. Vallet-Regi, Nanoparticles to knockdown osteoporosis-related gene and promote osteogenic marker expression for osteoporosis treatment. *ACS Nano* **13**, 5451–5464 (2019).
24. Y. Pang, Y. Fu, C. Li, Z. Wu, W. Cao, X. Hu, X. Sun, W. He, X. Cao, D. Ling, Q. Li, C. Fan, C. Yang, X. Kong, A. Qin, Metal-organic framework nanoparticles for ameliorating breast cancer-associated osteolysis. *Nano Lett.* **20**, 829–840 (2020).
25. R. Zhao, T. Shang, B. Yuan, X. Zhu, X. Zhang, X. Yang, Osteoporotic bone recovery by a bamboo-structured bioceramic with controlled release of hydroxyapatite nanoparticles. *Bioact. Mater.* **17**, 379–393 (2022).
26. T. Kitao, Y. Zhang, S. Kitagawa, B. Wang, T. Uemura, Hybridization of MOFs and polymers. *Chem. Soc. Rev.* **46**, 3108–3133 (2017).
27. J. Yang, Y. W. Yang, Metal-organic frameworks for biomedical applications. *Small* **16**, e1906846 (2020).
28. R. F. Mendes, F. Figueira, J. P. Leite, L. Gales, F. A. Almeida Paz, Metal-organic frameworks: A future toolbox for biomedicine? *Chem. Soc. Rev.* **49**, 9121–9153 (2020).
29. Y. Guo, Q. Sun, F. G. Wu, Y. Dai, X. Chen, Polyphenol-containing nanoparticles: Synthesis, properties, and therapeutic delivery. *Adv. Mater.* **33**, e2007356 (2021).
30. Y. Yang, W. Zhu, L. Feng, Y. Chao, X. Yi, Z. Dong, K. Yang, W. Tan, Z. Liu, M. Chen, G-quadruplex-based nanoscale coordination polymers to modulate tumor hypoxia and achieve nuclear-targeted drug delivery for enhanced photodynamic therapy. *Nano Lett.* **18**, 6867–6875 (2018).
31. Y. Yang, B. Liu, Y. Liu, J. Chen, Y. Sun, X. Pan, J. Xu, S. Xu, Z. Liu, W. Tan, DNA-based MXFs to enhance radiotherapy and stimulate robust antitumor immune responses. *Nano Lett.* **22**, 2826–2834 (2022).
32. M. Li, C. Wang, Z. Di, H. Li, J. Zhang, W. Xue, M. Zhao, K. Zhang, Y. Zhao, L. Li, Engineering multifunctional dna hybrid nanospheres through coordination-driven self-assembly. *Angew. Chem. Int. Ed. Engl.* **58**, 1350–1354 (2019).
33. Z. Zou, L. He, X. Deng, H. Wang, Z. Huang, Q. Xue, Z. Qing, Y. Lei, R. Yang, J. Liu, Zn^{2+}-coordination-driven rna assembly with retained integrity and biological functions. *Angew. Chem. Int. Ed. Engl.* **60**, 22970–22976 (2021).
34. S. Li, Q. Jiang, S. Liu, Y. Zhang, Y. Tian, C. Song, J. Wang, Y. Zou, G. J. Anderson, J. Y. Han, Y. Chang, Y. Liu, C. Zhang, L. Chen, G. Zhou, G. Nie, H. Yan, B. Ding, Y. Zhao, A DNA nanorobot functions as a cancer therapeutic in response to a molecular trigger in vivo. *Nat. Biotechnol.* **36**, 258–264 (2018).
35. D. H. Bunka, P. G. Stockley, Aptamers come of age—At last. *Nat. Rev. Microbiol.* **4**, 588–596 (2006).
36. J. Zhou, J. Rossi, Aptamers as targeted therapeutics: Current potential and challenges. *Nat. Rev. Drug Discov.* **16**, 181–202 (2017).
37. W. Sun, W. Ji, J. M. Hall, Q. Hu, C. Wang, C. L. Beisel, Z. Gu, Self-assembled DNA nanoclews for the efficient delivery of CRISPR-Cas9 for genome editing. *Angew. Chem. Int. Ed. Engl.* **54**, 12029–12033 (2015).
38. M. Farokhi, F. Mottaghitalab, S. Samani, M. A. Shokrgozar, S. C. Kundu, R. L. Reis, Y. Fatahi, D. L. Kaplan, Silk fibroin/hydroxyapatite composites for bone tissue engineering. *Biotechnol. Adv.* **36**, 68–91 (2018).
39. D. Zhang, X. Wu, J. Chen, K. Lin, The development of collagen based composite scaffolds for bone regeneration. *Bioact. Mater.* **3**, 129–138 (2018).
40. W. J. Boyle, W. S. Simonet, D. L. Lacey, Osteoclast differentiation and activation. *Nature* **423**, 337–342 (2003).
41. L. Tian, X. Yi, Z. Dong, J. Xu, C. Liang, Y. Chao, Y. Wang, K. Yang, Z. Liu, Calcium bisphosphonate nanoparticles with chelator-free radiolabeling to deplete tumor-associated macrophages for enhanced cancer radioisotope therapy. *ACS Nano* **12**, 11541–11551 (2018).
42. J. Chen, Y. Wang, W. Zhang, D. Zhao, L. Zhang, J. Fan, J. Li, Q. Zhan, Membranous NOX5-derived ROS oxidizes and activates local Src to promote malignancy of tumor cells. *Signal Transduct. Target. Ther.* **5**, 139 (2020).
43. W. Zhong, J. S. Yu, Y. Liang, Chlorobenzylidine-herring sperm DNA interaction: Binding mode and thermodynamic studies. *Spectrochim. Acta A Mol. Biomol. Spectrosc.* **59**, 1281–1288 (2003).
44. M. N. Patel, C. R. Patel, H. N. Joshi, Interaction of drug based copper(II) complexes with herring sperm DNA and their biological activities. *Spectrochim. Acta A Mol. Biomol. Spectrosc.* **97**, 66–73 (2012).
45. W. Yu, Y. Zheng, H. Li, H. Lin, Z. Chen, Y. Tian, H. Chen, P. Zhang, X. Xu, Y. Shen, The Toll-like receptor ligand, CpG oligodeoxynucleotides, regulate proliferation and osteogenic differentiation of osteoblast. *J. Orthop. Surg. Res.* **15**, 327 (2020).
46. A. Amcheslavsky, Z. Bar-Shavit, Interleukin (IL)-12 mediates the anti-osteoclastogenic activity of CpG-oligodeoxynucleotides. *J. Cell. Physiol.* **207**, 244–250 (2006).
47. W. Sun, C. Zhao, Y. Li, L. Wang, G. Nie, J. Peng, A. Wang, P. Zhang, W. Tian, Q. Li, J. Song, C. Wang, X. Xu, Y. Tian, D. Zhao, Z. Xu, G. Zhong, B. Han, S. Ling, Y. Z. Chang, Y. Li, Osteoclast-derived microRNA-containing exosomes selectively inhibit osteoblast activity. *Cell Discov.* **2**, 16015 (2016).
48. G. J. Thirukonda, S. Uehara, T. Nakayama, T. Yamashita, Y. Nakamura, T. Mizoguchi, N. Takahashi, K. Yagami, N. Udagawa, Y. Kobayashi, The dynamin inhibitor dynasore inhibits bone resorption by rapidly disrupting actin rings of osteoclasts. *J. Bone Miner. Metab.* **34**, 395–405 (2016).
49. B. Li, F. Yu, F. Wu, K. Wang, F. Lou, D. Zhang, X. Liao, B. Yin, C. Wang, L. Ye, Visual osteoclast fusion via a fluorescence method. *Sci. Rep.* **8**, 10184 (2018).
50. N. J. Horwood, J. Elliott, T. J. Martin, M. T. Gillespie, IL-12 alone and in synergy with IL-18 inhibits osteoclast formation in vitro. *J. Immunol.* **166**, 4915–4921 (2001).
51. C. Zannetti, P. Parroche, M. Panaye, G. Roblot, H. Gruffat, E. Manet, A. L. Debaud, J. Plumas, N. Vey, C. Caux, N. Bendriss-Vermare, U. A. Hasan, TLR9 transcriptional regulation in response to double-stranded DNA viruses. *J. Immunol.* **193**, 3398–3408 (2014).
52. M. Yao, X. Liu, D. Li, T. Chen, Z. Cai, X. Cao, Late endosome/lysosome-localized Rab7b suppresses TLR9-initiated proinflammatory cytokine and type I IFN production in macrophages. *J. Immunol.* **183**, 1751–1758 (2009).
53. M. Wu, W. Chen, Y. Lu, G. Zhu, L. Hao, Y. P. Li, Gα13 negatively controls osteoclastogenesis through inhibition of the Akt-GSK3β-NFATc1 signalling pathway. *Nat. Commun.* **8**, 13700 (2017).
54. K. Chen, P. Qiu, Y. Yuan, L. Zheng, J. He, C. Wang, Q. Guo, J. Kenny, Q. Liu, J. Zhao, J. Chen, J. Tickner, S. Fan, X. Lin, J. Xu, Pseurotin A inhibits osteoclastogenesis and prevents ovariectomized-induced bone loss by suppressing reactive oxygen species. *Theranostics* **9**, 1634–1650 (2019).
55. D. L. Lacey, W. J. Boyle, W. S. Simonet, P. J. Kostenuik, W. C. Dougall, J. K. Sullivan, J. San Martin, R. Dansey, Bench to bedside: Elucidation of the OPG-RANK-RANKL pathway and the development of denosumab. *Nat. Rev. Drug Discov.* **11**, 401–419 (2012).
56. A. C. Wu, L. J. Raggatt, K. A. Alexander, A. R. Pettit, Unraveling macrophage contributions to bone repair. *Bonekey Rep.* **2**, 373 (2013).
57. C. Schlundt, T. El Khassawna, A. Serra, A. Dienelt, S. Wendler, H. Schell, N. van Rooijen, A. Radbruch, R. Lucius, S. Hartmann, G. N. Duda, K. Schmidt-Bleek, Macrophages in bone fracture healing: Their essential role in endochondral ossification. *Bone* **106**, 78–89 (2018).
58. J. W. Lee, I. H. Lee, T. Iimura, S. W. Kong, Two macrophages, osteoclasts and microglia: From development to pleiotropy. *Bone Res.* **9**, 11 (2021).
59. P. Guihard, Y. Danger, B. Brounais, E. David, R. Brion, J. Delecrin, C. D. Richards, S. Chevalier, F. Redini, D. Heymann, H. Gascan, F. Blanchard, Induction of osteogenesis in mesenchymal stem cells by activated monocytes/macrophages depends on oncostatin M signaling. *Stem Cells* **30**, 762–772 (2012).
60. T. J. Fernandes, J. M. Hodge, P. P. Singh, D. G. Eeles, F. M. Collier, I. Holten, P. R. Ebeling, G. C. Nicholson, J. M. Quinn, Cord blood-derived macrophage-lineage cells rapidly

stimulate osteoblastic maturation in mesenchymal stem cells in a glycoprotein-130 dependent manner. *PLOS ONE* **8**, e73266 (2013).

61. K. B. Farrell, A. Karpeisky, D. H. Thamm, S. Zinnen, Bisphosphonate conjugation for bone specific drug targeting. *Bone Rep.* **9**, 47–60 (2018).
62. L. E. Cole, T. Vargo-Gogola, R. K. Roeder, Targeted delivery to bone and mineral deposits using bisphosphonate ligands. *Adv. Drug Deliv. Rev.* **99**, 12–27 (2016).
63. L. Xiong, J. U. Jung, H. Wu, W. F. Xia, J. X. Pan, C. Shen, L. Mei, W. C. Xiong, Lrp4 in osteoblasts suppresses bone formation and promotes osteoclastogenesis and bone resorption. *Proc. Natl. Acad. Sci. U.S.A.* **112**, 3487–3492 (2015).
64. T. Schinke, A. F. Schilling, A. Baranowsky, S. Seitz, R. P. Marshall, T. Linn, M. Blaeker, A. K. Huebner, A. Schulz, R. Simon, M. Gebauer, M. Priemel, U. Kornak, S. Perkovic, F. Barvencik, F. T. Beil, A. del Fattore, A. Frattini, T. Streichert, K. Pueschel, A. Villa, K. M. Debatin, J. M. Rueger, A. Teti, J. Zustin, G. Sauter, M. Amling, Impaired gastric acidification negatively affects calcium homeostasis and bone mass. *Nat. Med.* **15**, 674–681 (2009).
65. H. Zhao, J. Lv, F. Li, Z. Zhang, C. Zhang, Z. Gu, D. Yang, Enzymatical biomineralization of DNA nanoflowers mediated by manganese ions for tumor site activated magnetic resonance imaging. *Biomaterials* **268**, 120591 (2021).
66. C. Dou, N. Ding, F. Luo, T. Hou, Z. Cao, Y. Bai, C. Liu, J. Xu, S. Dong, Graphene-based MicroRNA transfection blocks preosteoclast fusion to increase bone formation and vascularization. *Adv. Sci.* **5**, 1700578 (2018).
67. H. Kim, K. Lee, J. M. Kim, M. Y. Kim, J. R. Kim, H. W. Lee, Y. W. Chung, H. I. Shin, T. Kim, E. S. Park, J. Rho, S. H. Lee, N. Kim, S. Y. Lee, Y. Choi, D. Jeong, Selenoprotein W ensures physiological bone remodeling by preventing hyperactivity of osteoclasts. *Nat. Commun.* **12**, 2258 (2021).
68. F. Jin, J. Li, Y. B. Zhang, X. Liu, M. Cai, M. Liu, M. Li, C. Ma, R. Yue, Y. Zhu, R. Lai, Z. Wang, X. Ji, H. Wei, J. Dong, Z. Liu, Y. Wang, Y. Sun, X. Wang, A functional motif of long noncoding RNA Nron against osteoporosis. *Nat. Commun.* **12**, 3319 (2021).

Acknowledgments

Funding: This work was supported by grants from the National Research Programs of China (no. 2022YFA1206500), the National Natural Science Foundation of China (nos. 22277072 and 22107065) and "Clinic Plus" Outstanding Project (nos. 2021ZYB009 and 2021ZYB003) from Shanghai Key Laboratory for Nucleic Acid Chemistry and Nanomedicine, and Innovative research team of high-level local universities in Shanghai. **Author contributions:** Conceptualization: J.X., Z. Li, Z. Liu, and Y.Y. Methodology: X.L., F.L., and Z.D. Validation: Y.Y., X.L., and F.L. Formal analysis: Z. Li, Z. Liu, Y.Y., and X.L. Investigation: X.L., F.L., Z.D., C.G., and D.M. Data curation: X.L. Writing (original draft): X.L. and Y.Y. Writing (review and editing): X.L., Y.Y., J.C., L.L., Y.H., and Z. Liu. Visualization: Y.Y. and X.L. Supervision: Z. Li, Z. Liu, and Y.Y. Project administration: Z. Li, Z. Liu, and Y.Y. Funding acquisition: J.X., Z. Li, Z. Liu, and Y.Y. **Competing interests:** The authors declare that they have no competing interests. **Data and materials availability:** All data needed to evaluate the conclusions in the paper are present in the paper and/or the Supplementary Materials.

Submitted 18 October 2022
Accepted 29 June 2023
Published 2 August 2023
10.1126/sciadv.adf3329